LBL-25141
Preprint

Lawrence Berkeley Laboratory
UNIVERSITY OF CALIFORNIA

Physics Division

Submitted to Astrophysical Journal

Formaldehyde Absorption toward W51

A. Kogut, G.F. Smoot, C.L. Bennett, and S.J. Petuchowski

April 1988

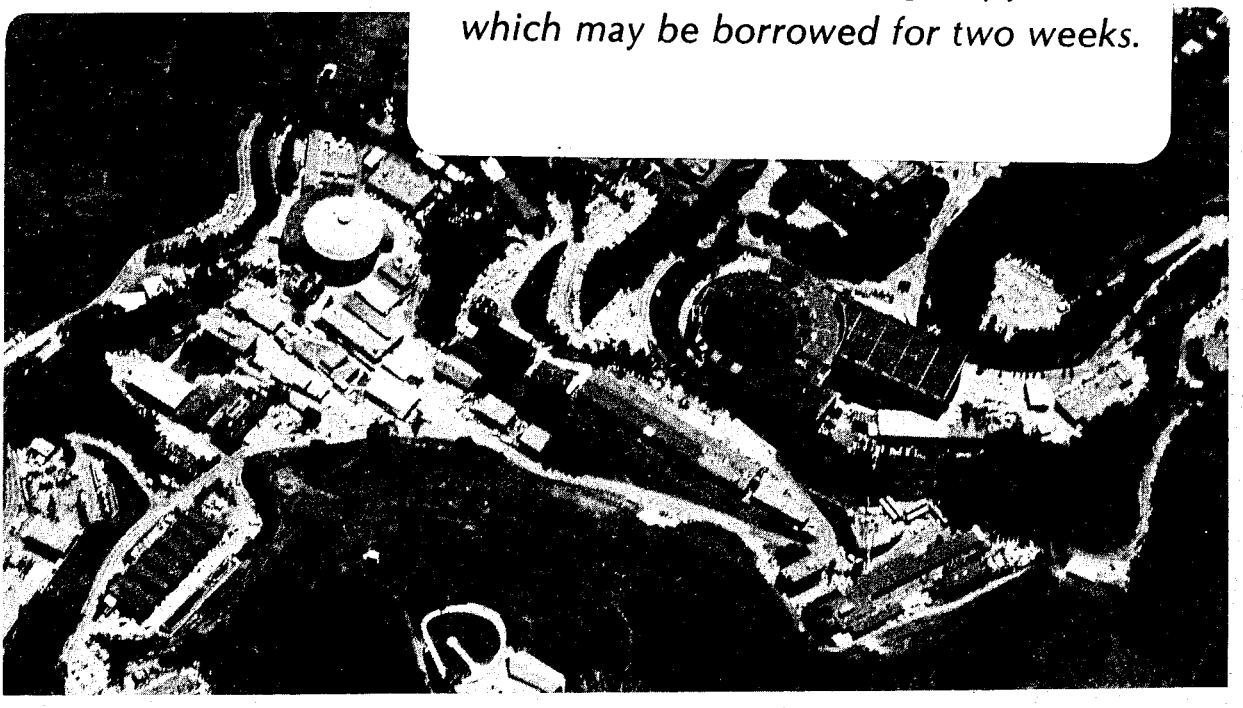

Prepared for the U.S. Department of Energy under Contract Number DE-AC03-76SF00098.

FORMALDEHYDE ABSORPTION TOWARD W51

A. KOGUT, G.F. SMOOT

Space Sciences Laboratory and Lawrence Berkeley Laboratory

University of California, Berkeley CA 94720

C.L. BENNETT, S.J. PETUCHOWSKI

Laboratory for Astronomy and Solar Physics

NASA Goddard Space Flight Center

Greenbelt MD 20771

ABSTRACT

We have measured formaldehyde (H_2CO) absorption toward the HII region complex W51A (G49.5-0.4) in the 6 cm and 2 cm wavelength rotational transitions with angular resolution of approximately 4". The continuum HII region shows a large, previously undetected shell structure 5.5 pc along the major axis. We observe no H_2CO emission in regions of low continuum intensity. The absorption, converted to optical depth, shows a higher degree of clumping than previous maps at lower resolution. The good S/N of the maps allows accurate estimation of the complicated line profiles, showing some of the absorbing clouds to be quite patchy. We list the properties of the opacity spectra for a number of positions both in the clumps and in the more diffuse regions of the absorbing clouds, and derive column densities for the 1_{11} and 2_{12} rotational levels of ortho-formaldehyde.

Subject headings: interstellar: molecules — nebulae: HII regions— nebulae: individual

I. INTRODUCTION

W51 is a giant HII region complex, located in the Sagittarius spiral arm at a distance of approximately 7.5 kpc (Genzel *et al.* 1981). A number of researchers have studied the radio continuum sources and the associated and foreground molecular clouds. Bieging (1975) has reviewed the morphology of the W51 complex; only a brief overview will be presented here. The W51 complex consists of a number of discrete sources in a diffuse continuum envelope. The brightest of these at wavelength 6 cm is W51A (G49.5-0.4). Martin (1972) identified eight components, designated a through h, in the λ = 6 cm wavelength radio continuum of W51A. Of these, the two brightest (d and e) are associated with near-infrared sources IRS2 and 1, respectively (Wynn-Williams *et al.* 1974, Genzel *et al.* 1982). Scott (1978) has mapped interferometrically the radio continuum about W51d and e, and found two compact sources 1' to the east of the peak W51e, designated W51e_1 and e_2. The areas near W51e_1, e_2, and IRS2 are rich sources of maser activity in OH (Mader *et al.* 1978), H_2O (Genzel et al. 1982), and of emission from hot NH_3 (Mauersberger *et al.* 1987).

Transitions between the low-lying rotational states of ortho-formaldehyde are a useful probe of conditions within molecular clouds. W51A has been extensively studied in the λ=6 cm wavelength ($1_{10}\leftarrow1_{11}$) transition (Arnal and Goss 1985, Martin-Pintado *et al.* 1985), and to lesser resolution in the λ=2 cm wavelength ($2_{11}\leftarrow2_{12}$) transition (Gardner and Whiteoak 1984), and λ=2 mm transitions (Wilson and Jaffe 1981). The results have been used to establish the degree of clumping and turbulence in the absorbing clouds, the local H_2 density, and the relative positions of the clouds and continuum sources. The situation is complicated by the extreme projection effects; at galactic longitude 49°, the line of sight through the Sagittarius spiral arm is nearly 5 kpc.

Comparison of results at different wavelengths has been hampered by differing resolution and sensitivity. In this paper, we present new interferometric maps of H_2CO absorption toward W51A, of similar resolution and sensitivity in both the 6 and 2 cm transitions of ortho-formaldehyde. We show a

new, large shell structure in the continuum to the SW of W51e, apparently connected to the discrete source W51b. The absorption, converted to optical depth, shows significant clumping on the scale of the synthesized beamwidth over most, but not all, of the sources.

II. OBSERVATIONS

We observed the 6 cm transition of ortho-formaldehyde (rest frequency 4.8296596 GHz) on November 8, 1986 using the Very Large Array (VLA) of the NRAO[1] in the C configuration. Spectral

---

[1] The National Radio Astronomy Observatory is operated by Associated Universities, Inc., under contract with the National Science Foundation.

---

coverage consisted of the inner 32 channels of a 256-channel, 3.125-MHz bandpass centered at 65.0 km s^{-1} LSR; the velocity resolution was 0.76 km s^{-1}. A total of 5.5 hours was spent on source. We calibrated the flux scale using an assumed value of 7.46 Jy for 3C286, and used a 0.5 hr integration of 3C84 to calibrate the bandpass. Phase calibration used 1923+210, observed for 5 minutes of every 30.

We observed the 2 cm transition (rest frequency 14.488479 GHz) on May 1, 2, and 3, 1987, with the VLA in the D configuration. Spectral coverage consisted of the inner 32 channels of a 128-channel, 3.125-MHz bandpass, again centered at 65.0 km s^{-1} LSR, for velocity resolution of 0.51 km s^{-1}. A total of 14.5 hours was spent on source, slightly less than expected owing to a power failure at the VLA site on May 3. We calibrated the flux scale using a value for 3C286 of 3.53 Jy. As with the 6 cm observations, we used a 1.5 hr integration of 3C84 for bandpass calibration and 1923+210, observed 5 minutes of every 30, for phase calibration. Table 1 lists observing parameters for both the 6 cm and 2 cm observations.

III. DATA REDUCTION

We employed standard VLA calibration and data reduction software to convert the observed visibilities to intensity maps. The three days of 2 cm observation were calibrated independently before being combined into a single visibility database. The dirty maps were CLEANed and the CLEAN components used as input for self-calibration of the phases.

For either frequency, Channel Zero contained the average of the inner three-quarters of the originally available passband. The velocity range covered had significant absorption in most channels; these channels formed a non-negligible fraction of Channel Zero. Accordingly, we formed a continuum map at both 6 and 2 cm by subtracting the suitably weighted average of the 31 data channels from Channel Zero. We then applied a correction for primary beam effects, a significant effect at 2 cm where the primary HPBW was approximately the size of the area of interest.

As with any interferometer, the VLA's sensitivity to large-scale structure is determined by the shortest baselines available and the details of the source structure. W51 is known to have considerable extended emission surrounding the compact sources (Bieging *et al.* 1982, Gardner and Whiteoak, 1984). Our continuum maps contained 48% and 55%, respectively, of the flux observed by single-dish measurements at 6 and 2 cm wavelength. We added the "missing" flux as a constant across the continuum maps; this amounted to 9.8 mJy/beam at 6 cm and 17.8 mJy/beam at 2 cm. The resultant continuum maps have an RMS noise of 1.5 mJy/beam at 6 cm, and 3 mJy/beam at 2 cm.

We produced dirty maps for each spectral channel, as well as a dirty continuum map (without the corrections described above). The absorption maps are the differences between the dirty channel maps and the continuum, CLEANed and corrected for the primary beam pattern. The absorption maps have RMS noise of 4 mJy/beam at 6 cm and 7 mJy/beam at 2 cm. We then made maps of the optical depth of the formaldehyde lines in the usual fashion. To prevent systematic uncertainties in the subtraction or the

continuum from affecting the results, we blanked the optical depth maps wherever corrections to the continuum for missing flux were more than 10% of the continuum.

IV. RESULTS

a) Continuum

The continuum maps are shown in Figures 1 and 2. The 6 cm continuum shows a large, low-level shell structure, not previously observed, which forms a continuation of the elongated compact source W51b. The shell does not show up clearly in the 2 cm continuum, which is somewhat less sensitive to weak diffuse features. The structure at 6 cm is well above the RMS noise, and does not correspond to the known sidelobe response of the array. It is 2.5' along the major axis, which, at a distance of 7.5 kpc, corresponds to a linear dimension 5.5 pc. The smooth connection with W51b suggests that W51b is a remnant of the process which formed the shell, in which a new burst of star formation has occurred.

Fitted intensities for selected features in the continuum maps are shown in Table 2. The ultra-compact region W51e_2 is detectable as a weak bump in the continuum emission in the 6 cm map; neither e_1 nor e_2 are resolved at either frequency.

b) Absorption

Absorption maps of the d and e features from selected channels are shown in Figures 3 and 4. For clarity, the contour plots have been blanked in regions where the absorption is less than three times the RMS noise level. The large changes in absorption from velocities only a few km s^{-1} apart are indicative of the complicated morphology of this region.

A notable feature of these maps is the lack of any formaldehyde emission in regions where the diffuse continuum emission is weak. Under conditions of high H_2 density ($n_{H2} > 10^6$ cm^{-3}), the H_2CO transitions are expected to thermalize, and could conceivably appear in emission on small scales. The absorption maps show no emission features inconsistent with the noise level of the maps. At the 95% confidence level, this places limits on any small-scale emission features to <7.8 mJy/beam at 6 cm and <11.8 mJy/beam at 2 cm.

c) Optical Depth

Contour plots of the optical depth in selected channels toward W51d and W51e are presented in Figures 5 and 6. We have blanked the maps in areas in which corrections to the continuum for "missing" flux amount to more than 10% of the uncorrected intensity.

Although several regions show relatively small, smooth variations, the opacity is dominated by clumping on angular scales of the beamwidth (4"), corresponding to linear scales of 0.15 pc. The opacity increases to the W and NW of W51e and to the N of W51d, in qualitative agreement with the results of Arnal and Goss (1985) and Martin-Pintado *et al.* (1985). In general, we derive higher opacity in the clump peaks, as would be expected for our finer angular resolution in the presence of clumping.

The absorption is clumped in velocity as well as position. The spectra show considerable velocity structure with several superposed features often contributing to a broad (>2 km s^{-1} FWHM) linewidth. We have fit gaussian profiles to the opacity spectra, using two gaussians in regions where this significantly improved the fit to the data. The resultant velocity centroids, binned and grouped by position to offset the variable sizes of the brighter continuum regions, are shown in Figure 7.

A number of features are apparent in figures 5—7. A diffuse feature at 66 km s-1 extends in patches over most of the source. A moderately strong feature at 64.5 km s^{-1} LSR dominates the northern portion of W51e, and extends in patches through the southern portion and into the region near W51d. A strong, ridged feature at 65.4 km s^{-1} dominates the central portion of W51e; this region is further complicated by velocity and spatial blending of the 64.5 and 65—66 km s^{-1} features. A strongly clumped feature at 69.6 km s^{-1} dominates the opacity toward the southernmost portion of W51e; in addition, a weaker, more diffuse feature at 67.4 km s^{-1} appears both here and toward W51d. Results from fitted gaussian profiles show significant variation in the velocity centroids over distances of a few arcmin. The variations are consistent at both frequencies and seem more indicative of patchiness and clumping than of large-scale motion of the absorbing clouds.

The absorption toward W51d also shows significant velocity blending. The dominant velocity structure occurs at 64, 66—67.5, and 68.5 km s^{-1}. Little positional clumping is apparent, only relatively smooth gradients to the N and E. This is consistent with the relatively smooth nature of the clouds seen toward the north of W51e.

V. DISCUSSION

Table 3 contains a summary of the observed spectra in the absorbing clouds. "Clump centers" refer to positions of local maxima of opacity for velocity centroids near a centroid peak (Fig 7). For each velocity centroid, we locate the position of the maxima from the fitted spectra gridded in 2"x2" bins. Since the opacity is not smooth on the scale of a few beamwidths, only those positions with local opacity increase greater than two are taken as clumps. Positions "off-clump" are a sampling of minimum-opacity regions and regions of typical "ambient" opacity. The velocity centroid (col 3), full width at half maximum (col 4), and optical depths in the doublet transitions (col 5 and 6) are taken from gaussian fits to the spectra. Typically, the velocity centroid and width are uncertain to ±0.2 km s^{-1}, while the opacities at 6 and 2 cm are uncertain to ±0.008 and ±0.004, respectively. Systematic uncertainties from such factors as uncertainty in the continuum owing to "missing" flux density in the interferometric maps have not been explicitly included in these error estimates. An uncertainty of 50% in the added flux contributes less than 5% uncertainty to the optical depths presented; the effect largely cancels in comparison of the 6 cm and 2 cm results.

We have converted the optical depth to H_2CO column density N_1 in the lower (1_{11}) level of the 6 cm transition using the relation (Arnal *et al.* 1982)

$$W_{6cm} = \frac{8\pi^3}{6h} |\mu_{6cm}|^2 N_1 \left[1 - \exp\left(\frac{-h\nu_{6cm}}{kT_{6cm}}\right) \right], \qquad (1)$$

where μ_{6cm} is the dipole transition moment of the 6 cm transition, ν is the frequency, T_{6cm} is the excitation temperature of the 6 cm transition, h is Planck's constant, and k is Boltzmann's constant. W_{6cm} is the opacity in the 6 cm transition integrated over velocity,

$$W = \int (1 - e^{-\tau}) \, dv, \qquad (2)$$

calculated from the fitted spectra. The column density in the 2_{12} level of the 2 cm transition , N_2, may be calculated from Eq. (1) by frequency-scaling the transition moment $|\mu|^2$.

The column densities in the two transitions (col 7 and 8 of Table 3) have been calculated from the fitted spectra. There is generally excellent agreement between the velocity centroids and widths in the two transitions; we use the more sensitive 6 cm FWHM to derive the equivalent widths *W*. At moderate H_2 densities ($10^2 \leq n \leq 10^5$ cm^{-3}), collisional pumping reduces the excitation temperatures T_{6cm} and T_{2cm} to subthermal values, typically 1.7 to 2.5 K (Garrison *et al.* 1975). Since there is no accurate estimation of these temperatures toward W51, the temperature dependence has been left explicit in the column densities in Table 3. No correction has been made for beam effects on clumps of size comparable to the beamwidth. The "ambient" absorption has not been subtracted from the clump positions; the quoted column densities are thus an upper limit to the densities of the clumps themselves.

Estimates of local conditions in the clump (H_2CO and H_2 density, mm wavelength excitation temperature) may be calculated from the opacity spectra, but are subject to uncertainty in a number of assumptions (*e.g.*, spherical symmetry, temperature of the cm-wavelength transitions, collisional excitation). In a forthcoming paper, we will present estimates of the hydrogen density and the 2 mm wavelength excitation temperatures in the absorbing clouds toward W51A, using the 6 and 2 cm wavelength opacities from this paper.

VI. CONCLUSIONS

We have mapped the absorption of ortho-formaldehyde toward W51A in both the 6 cm and 2 cm wavelength transitions. The source shows a complicated morphology, including a large, dim shell structure in the continuum and patchy, highly clumped absorption. Small-scale emission features are limited to <7.8 mJy/beam at 6 cm wavelength and <11.8 mJy/beam at 2 cm (95% confidence level). We derive the column density N_{H2CO} in the first (1_{11}) and third (2_{12}) rotational energy levels.

ACKNOWLEDGEMENTS

We thank M. Goss and J. Van Gorkom for useful advice at the VLA. H. Liszt (NRAO) provided help using CLEAN algorithms on sources containing both bright regions and diffuse continuum. The VLA array operators proved quite resourceful in enabling us to take data after a power outage damaged a number of the controlling computers. Partial funding for this project has been provided by DOE contract DEAC03-76-SF00098, NASA contract NAS5-27592, and NASA RTOP 188-41-55-07.

REFERENCES

Arnal, E.M., Goss, W.M., Dickel, H.R., and Forster, J.R. 1982, *M.N.R.A.S.* **210**, 317.

-----, and Goss, W.M. 1985, *Astron. Astrophys.* **145**, 369.

Bieging, J. 1975, *HII regions and related topics*, eds Wilson, T.L. and Downes, D., Springer-Verlag.

---, Wilson, T.L., and Downes, D. 1982, *Astron. Astrophys. Suppl. Ser.* **49**, 607.

Gardner, F.F., and Whiteoak, J.B. 1984, *M.N.R.A.S.* **210**, 23.

Garrison, B.J., Lester, W.A., Jr., Miller, W.H., and Green, S. 1975, *Ap. J.* **200**, L175.

Genzel, R. *et al.* 1981, *Ap. J.* **247**, 1039.

--- 1982, *Ap. J.* **255**, 527.

Ho, P.T.P., Genzel, R., and Das, A. 1983, *Ap. J.* **266**, 596.

Mader, G.L., Johnston, K.J., and Moran, J.M. 1978, *Ap. J.* **224**, 115.

Martin, A.H.M. 1972, *M.N.R.A.S.* **157**, 31.

Martin-Pintado, J., Wilson, T.L., Johnston, K.J., and Henkel, C. 1985, *Ap. J.* **299**, 386.

Mauersberger, R., Henkel, C., and Wilson, T.L. 1987, *Astron. Astrophys.* **173**, 352.

Scott, P.F. 1978, *M.N.R.A.S.* **183**, 435.

Wilson, T.L., Mezger, P.M., Gardner, FF., Milne, D.K. 1970, *Astrophys. Lett.* **5**, 99.

Wilson, T.L., and Jaffe, D.T. 1981, *Ap. J.* **245**, 866.

Wynn-Williams, C.G., Becklin, E.E., and Neugebauer, G. 1974, *Ap. J.* **187**, 473.

FIGURE CAPTIONS

Figure 1. The 6 cm wavelength continuum toward W51A (G49.5-0.4). The map has been CLEANed and corrected for the primary beam pattern. Contours are at 10, 20, 40, 100, 200, 400, 800, and 1200 mJy/beam. The beam shape is indicated by the black oval to the upper left.

Figure 2. The 2 cm wavelength continuum toward W51A. Similar corrections have been applied as for Figure 1. The first six contours are at 30, 50, 80, 150, 250, and 500 mJy/beam; successive contours are at 300 mJy/beam intervals. The designations of Martin (1972) are indicated. The beam shape is indicated by the black oval to the upper left.

Figure 3. Absorption maps at selected channels for the 6 cm wavelength transition. The LSR velocity of each map is indicated in the lower right corner. Contours are at 12, 50, 100, 200, 300, and 400 mJy/beam. The plots have been blanked in regions where the absorption is less than three times the RMS noise, and have been corrected for the primary beam pattern. The beam size is indicated by the black oval to the lower left. The reference position for Figures 3—6 is at $\alpha=19^h\ 21^m\ 24^s$, $\delta=14^\circ\ 24'\ 45''$ (1950.0).

Figure 4. Absorption maps at selected channels for the 2 cm wavelength transition. The LSR velocity of each map is indicated in the lower right corner. Contours are at 20, 40, 60, 80, 100, and 150 mJy/beam. The plots have been blanked in regions where the absorption is less than three times the RMS noise, and have been corrected for the primary beam pattern. The beam size is indicated by the black oval to the lower left.

Figure 5. Maps of the optical depth in selected channels of the 6 cm transition. The LSR velocity of each plot is indicated in the upper left corner. The lowest contour is at 0.0 opacity; successive contours are spaced by 0.1 to a maximum of 1.2. The grey scale distinguishes regions of increasing and decreasing opacity; selected contours are labelled. The beam size is indicated by the shaded oval at the bottom right corner of the first plot.

Figure 6. Maps of the optical depth in selected channels of the 2 cm transition. The LSR velocity of each plot is indicated in the upper left corner. The contours are as in Figure 5. The beam size is indicated by the shaded oval at the bottom right corner of the first plot.

Figure 7. Histograms of the velocity distribution of the absorbing clouds. The area from which each plot was taken is indicated in the upper right corner of the first plot. The data were taken from a 2"x2" grid over the absorbing regions. The size of the peaks in the distribution are proportional to the area of the feature at that velocity.

A. Kogut and G.F. Smoot: 50/232 Lawrence Berkeley Laboratory, University of California, Berkeley, CA 94720.

C.L. Bennett and S.J. Petuchowski: Code 685, Laboratory for Astronomy and Solar Physics, Goddard Space Flight Center, Greenbelt, MD 20771.

TABLE 1

OBSERVING PARAMETERS

		6 cm	2 cm
Observing Dates		1986 Nov 8	1987 May 1,2,3
Telescope		VLA, C configuration	VLA, D configuration
Number of antennas		25	25
Phase center	α_0 (1950.0)	$19^h\ 21^m\ 19.^s0$	$19^h\ 21^m\ 22.^s5$
	δ_0 (1950.0)	14d 24' 30"	14d 24' 30"
Integration time		5.5 hr	14.5 hr
Primary HPBW		9'	3'
Area Mapped		8.5' x 8.5' (α x δ)	4.3' x 4.3' (α x δ)
Synthesized HPBW		4.14" x 3.59" (α x δ)	3.73" x 3.66" (α x δ)
Rest frequency		4.8296596 GHz	14.488479 GHz
Number of channels		32	32
Channel width		12.207 kHz	24.414 kHz
Velocity resolution		0.76 km s^{-1}	0.51 km s^{-1}
Lowest channel		53.6 km s^{-1}	57.4 km s^{-1}
Highest channel		76.4 km s^{-1}	72.6 km s^{-1}

TABLE 2

CONTINUUM INTENSITY

Feature	Intensity (mJy/beam)	
	6 cm	2 cm
W51d	1223±16	1970±29
W51e	779±25	830±31
W51b	198±5	162±3
$W51e_1$	125±9	155±6
$W51e_2$	48±4	177±6

TABLE 3

SUMMARY OF OPACITY SPECTRA

Position		V	FWHM	Optical Depth		Column Density [a]	
α(1950.0)	δ(1950.0)	(km s^{-1})	(km s^{-1})	6 cm	2 cm	N_1	N_2
(1)	(2)	(3)	(4)	(5)	(6)	(7)	(8)
W51e, Clump Centers							
$19^h\ 21^m\ 24.^s73$	14° 25' 1"	64.5	3.3	0.357	0.102	1.39	0.43
$19^h\ 21^m\ 25.^s00$	14° 24' 39"	65.0	2.7	1.148	0.299	2.90	0.98
$19^h\ 21^m\ 24.^s47$	14° 24' 45"	65.4	2.9	0.701	0.253	2.18	0.91
$19^h\ 21^m\ 24.^s20$	14° 24' 41"	65.4	3.2	0.640	0.188	2.24	0.77
$19^h\ 21^m\ 23.^s79$	14° 24' 47"	64.4	2.6	0.449	0.266	1.34	0.85
		66.9	2.1	0.370	0.131	0.94	0.36
$19^h\ 21^m\ 24.^s47$	14° 24' 29"	66.0	2.3	0.306	0.159	0.84	0.46
		69.6	1.7	0.578	0.263	1.09	0.55
$19^h\ 21^m\ 24.^s47$	14° 24' 9"	67.4	2.5	0.338	0.084	0.99	0.27
W51e, Off-Clump							
$19^h\ 21^m\ 25.^s53$	14° 25' 5"	64.2	4.7	0.161	<0.03	0.98	<0.2
$19^h\ 21^m\ 24.^s33$	14° 24' 55"	65.2	3.8	0.142	0.028	0.70	0.14
$19^h\ 21^m\ 23.^s79$	14° 24' 43"	65.3	5.8	0.333	0.19	2.29	1.3
$19^h\ 21^m\ 24.^s33$	14° 24' 17"	65.8	1.9	0.121	0.042	0.29	0.10
$19^h\ 21^m\ 24.^s73$	14° 24' 7"	67.1	1.8	0.116	<0.01	0.27	<0.05
W51d, Clump Centers							
$19^h\ 21^m\ 22.^s33$	14° 25' 21"	64.5	4.0	0.24	0.08	1.19	0.44
		67.5	3.4	0.30	0.10	1.24	0.46
$19^h\ 21^m\ 21.^s97$	14° 25' 15"	68.3	1.9	0.223	0.114	0.51	0.27
		63.4	3.5	0.055	0.023	0.26	0.11
W51d, Off-Clump							
$19^h\ 21^m\ 22.^s07$	14° 25' 19"	66.0	5.2	0.232	0.100	1.51	0.68
		68.4	1.7	0.17	<0.01	0.38	<0.05
$19^h\ 21^m\ 25.^s44$	14° 25' 3"	64.4	3.0	0.280	0.087	1.02	0.34

[a] Column densities are in units 10^{13} cm^{-2} K^{-1}

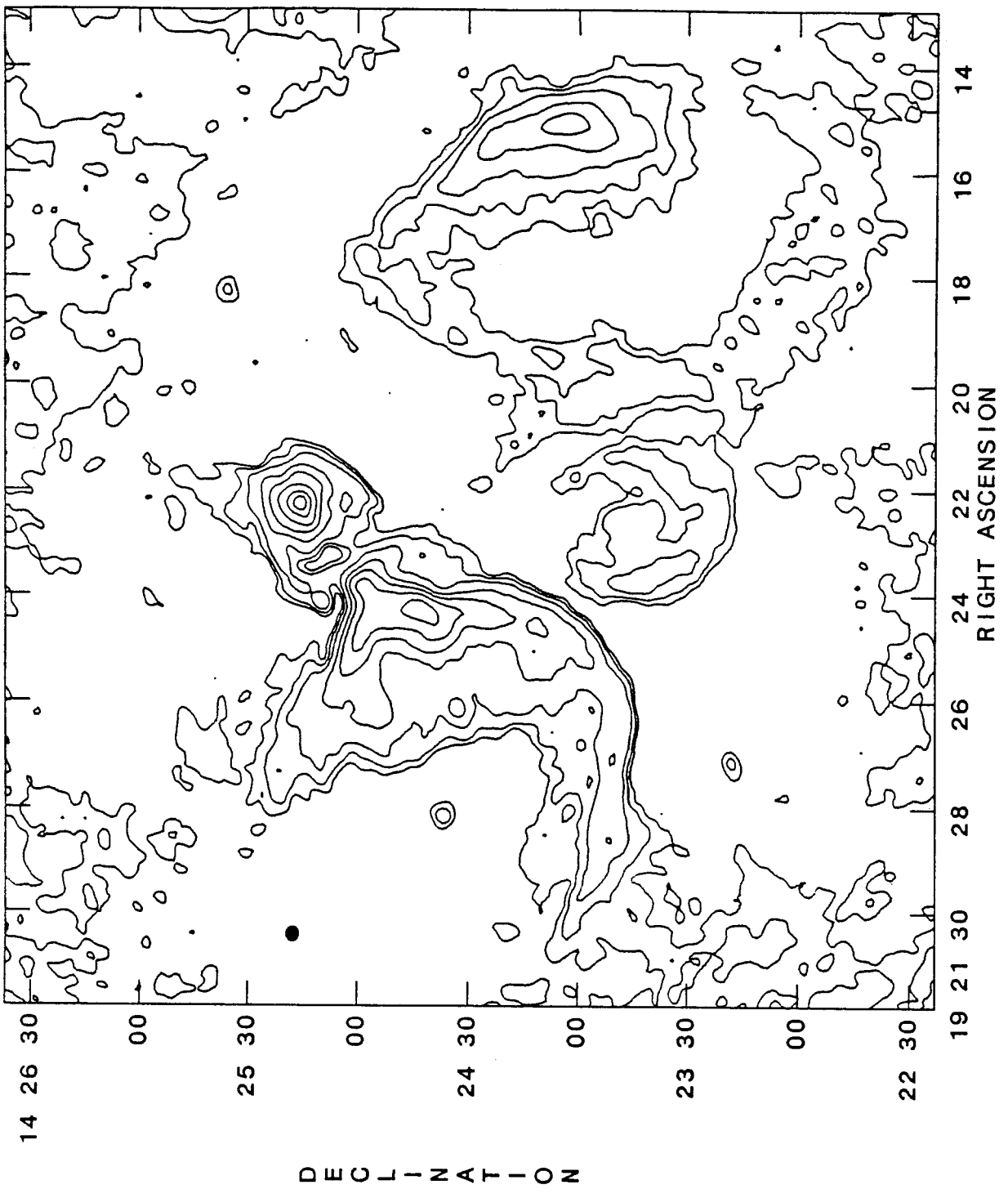
DECLINATION
14 26 30
00
25 30
00
24 30
00
23 30
00
22 30
19 21 30
28
26
24
22
20
18
16
14
RIGHT ASCENSION

Fig. 1

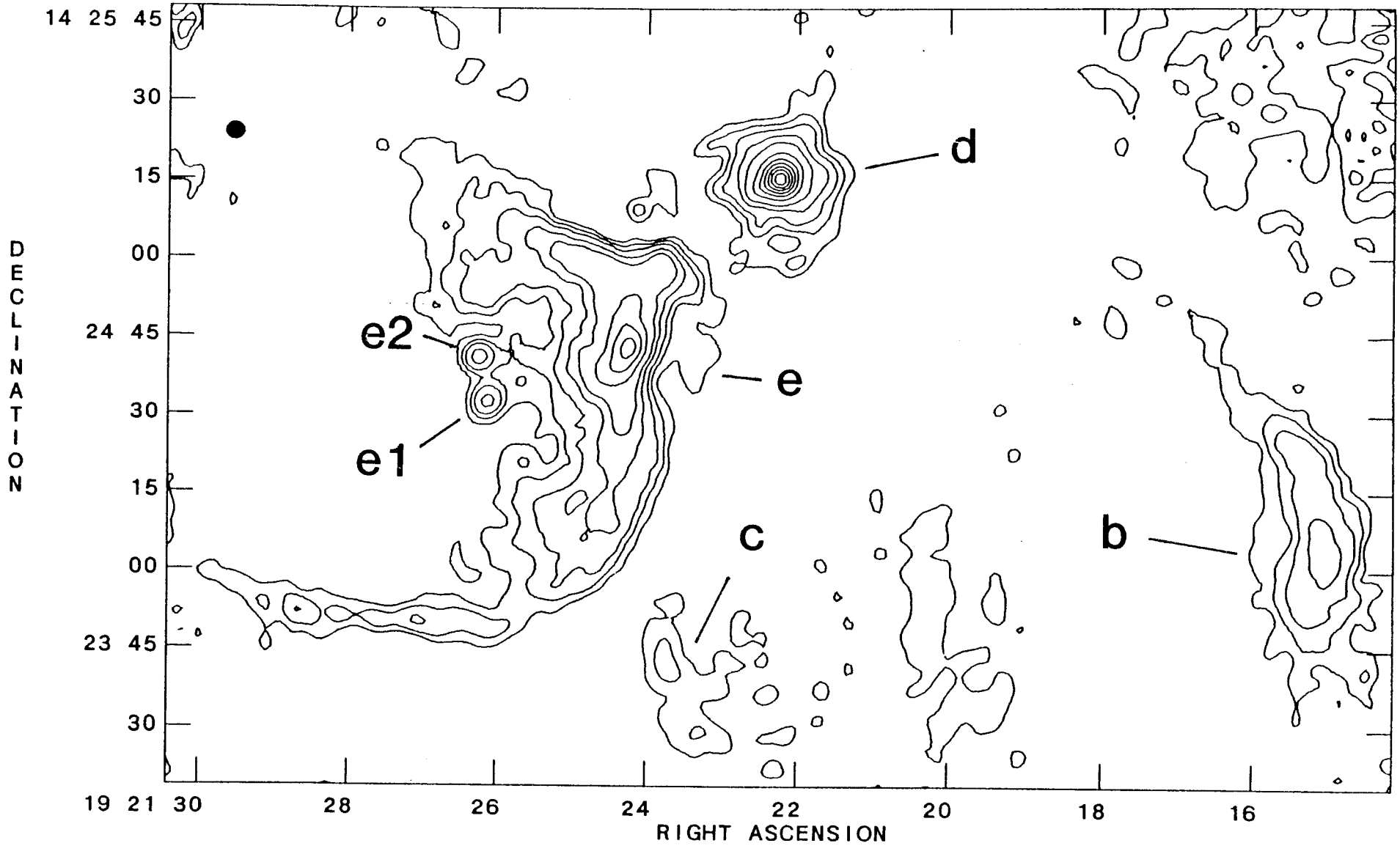
14 25 45
30
15
00
24 45
30
15
00
23 45
30
DECLINATION
19 21 30
28
26
24
22
20
18
16
RIGHT ASCENSION
d
e2
e
e1
c
b

Fig. 2

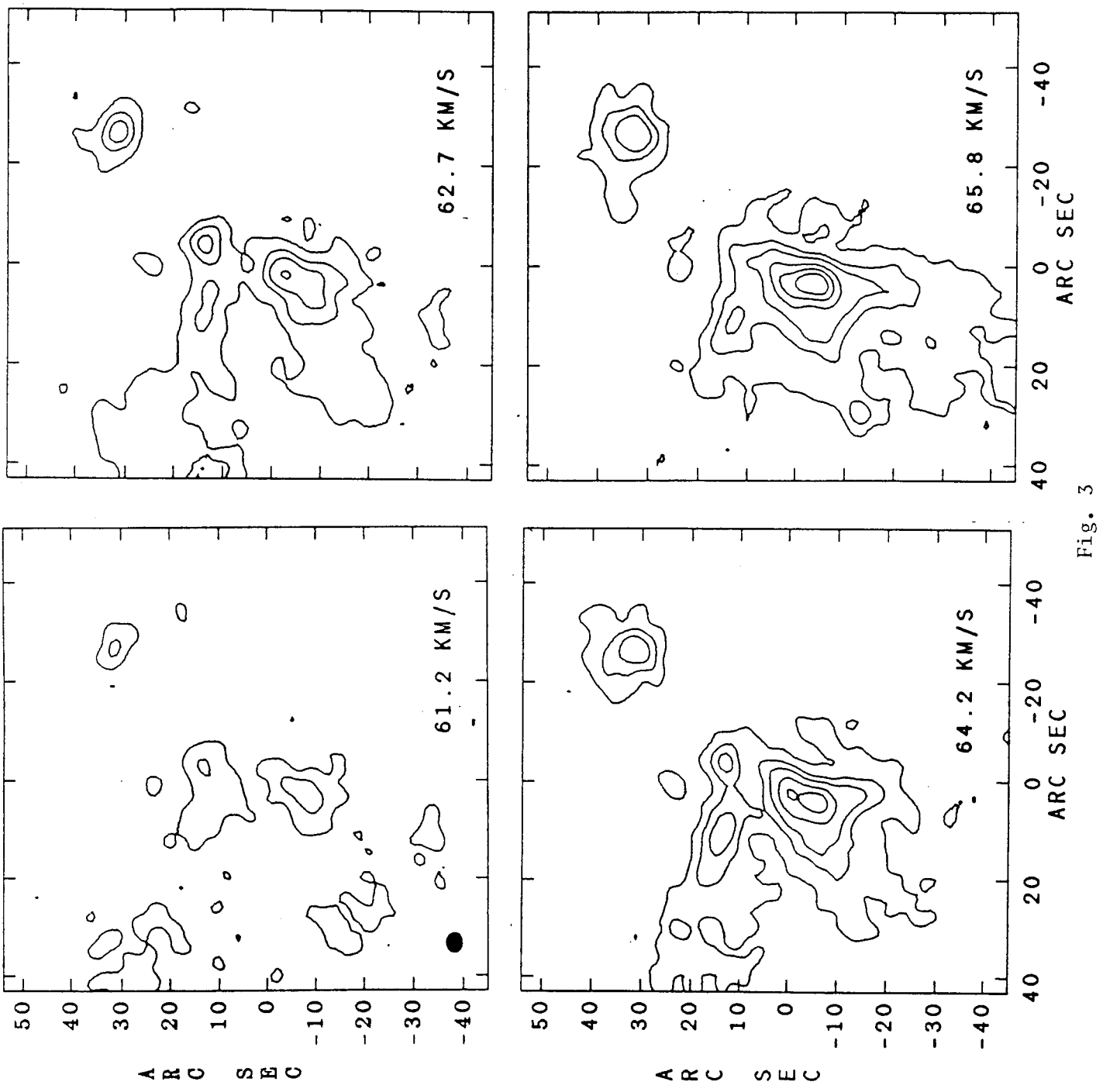
61.2 KM/S
62.7 KM/S
64.2 KM/S
65.8 KM/S
ARC SEC
ARC SEC
50
40
30
20
10
0
-10
-20
-30
-40

Fig. 3

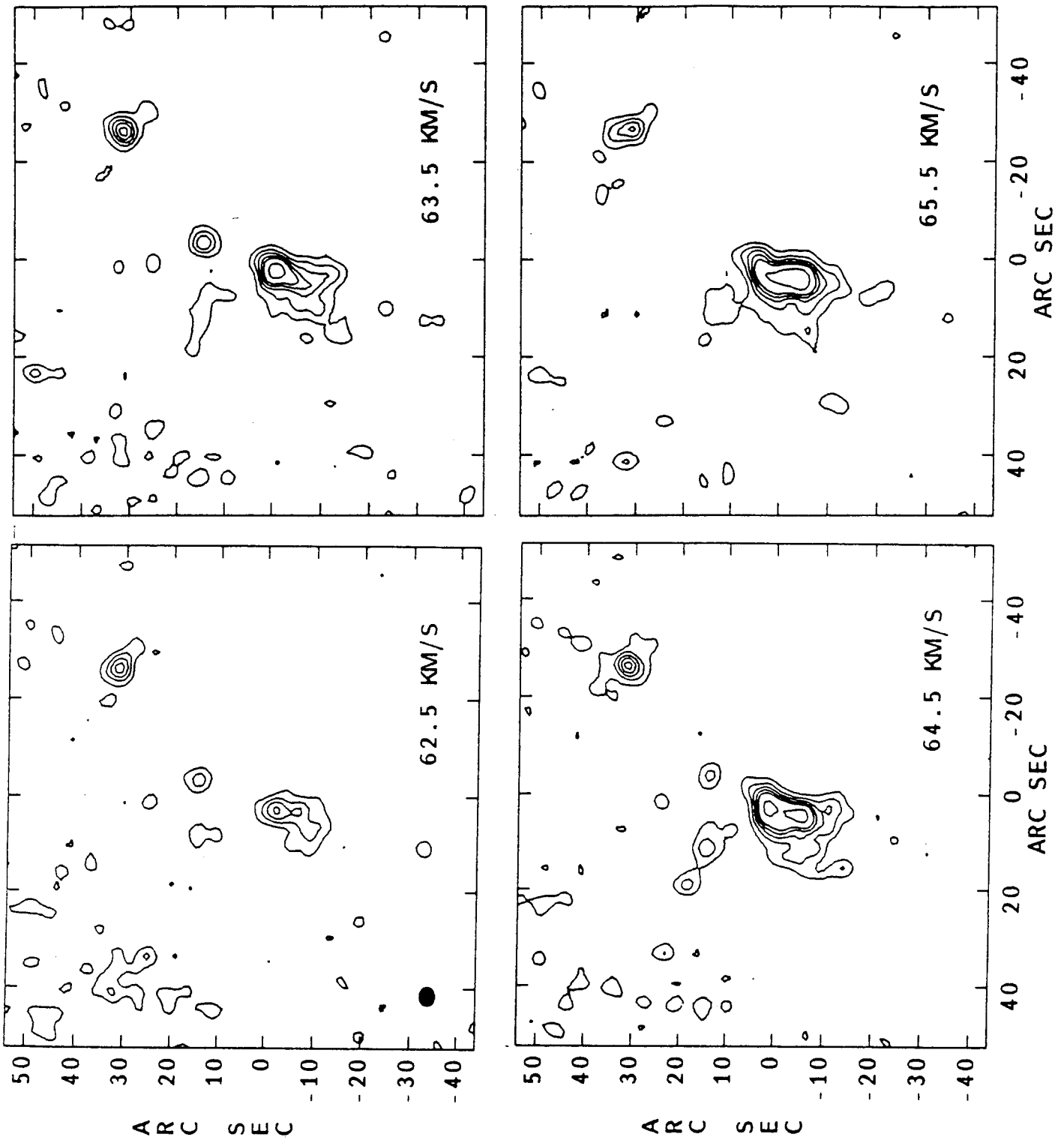
63.5 KM/S
62.5 KM/S
65.5 KM/S
64.5 KM/S
ARC SEC
ARC SEC
50
40
30
20
10
0
-10
-20
-30
-40
40
20
0
-20
-40

Fig. 4

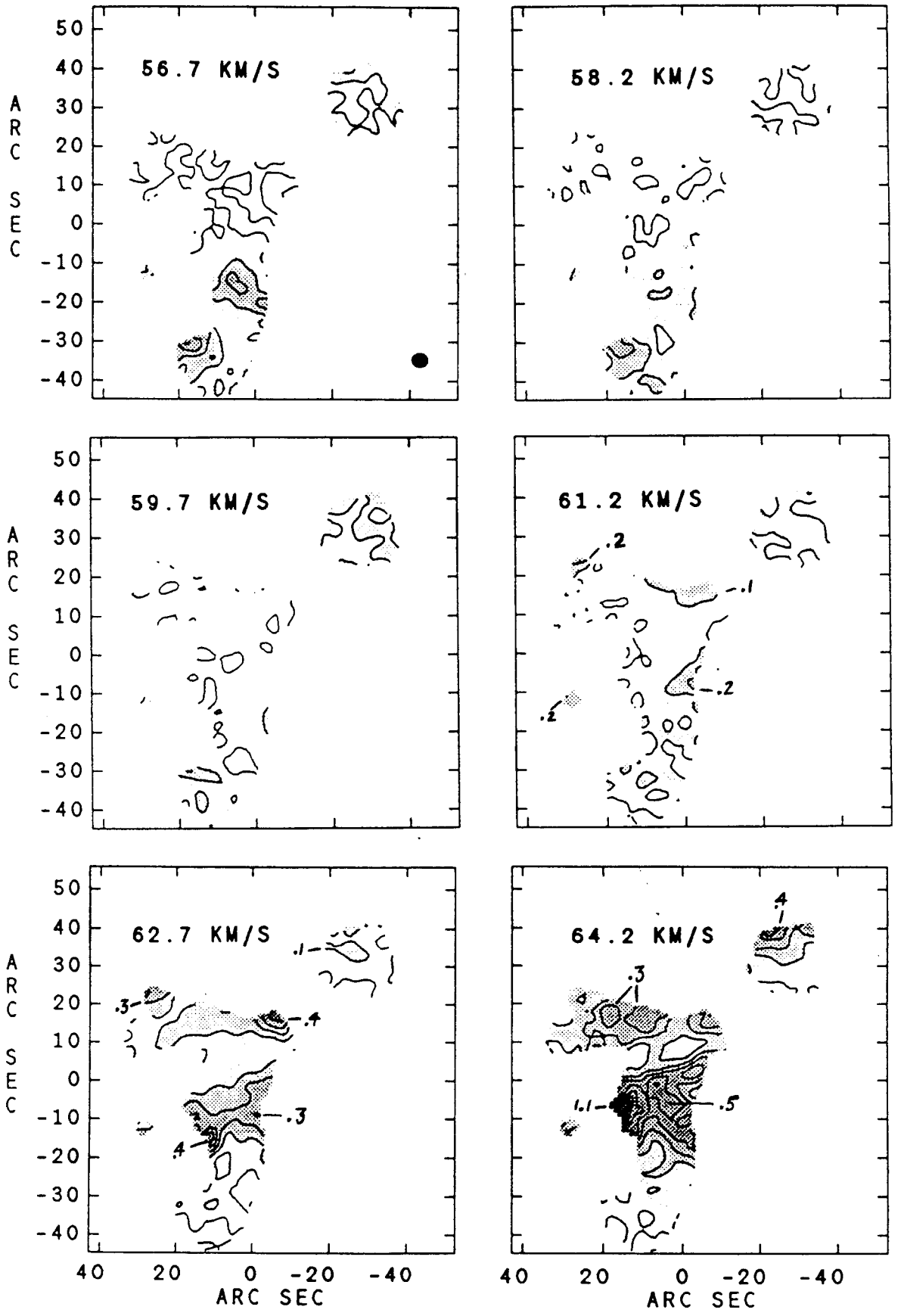
56.7 KM/S
58.2 KM/S
59.7 KM/S
61.2 KM/S
62.7 KM/S
64.2 KM/S
ARC SEC
50
40
30
20
10
0
-10
-20
-30
-40

Fig. 5a

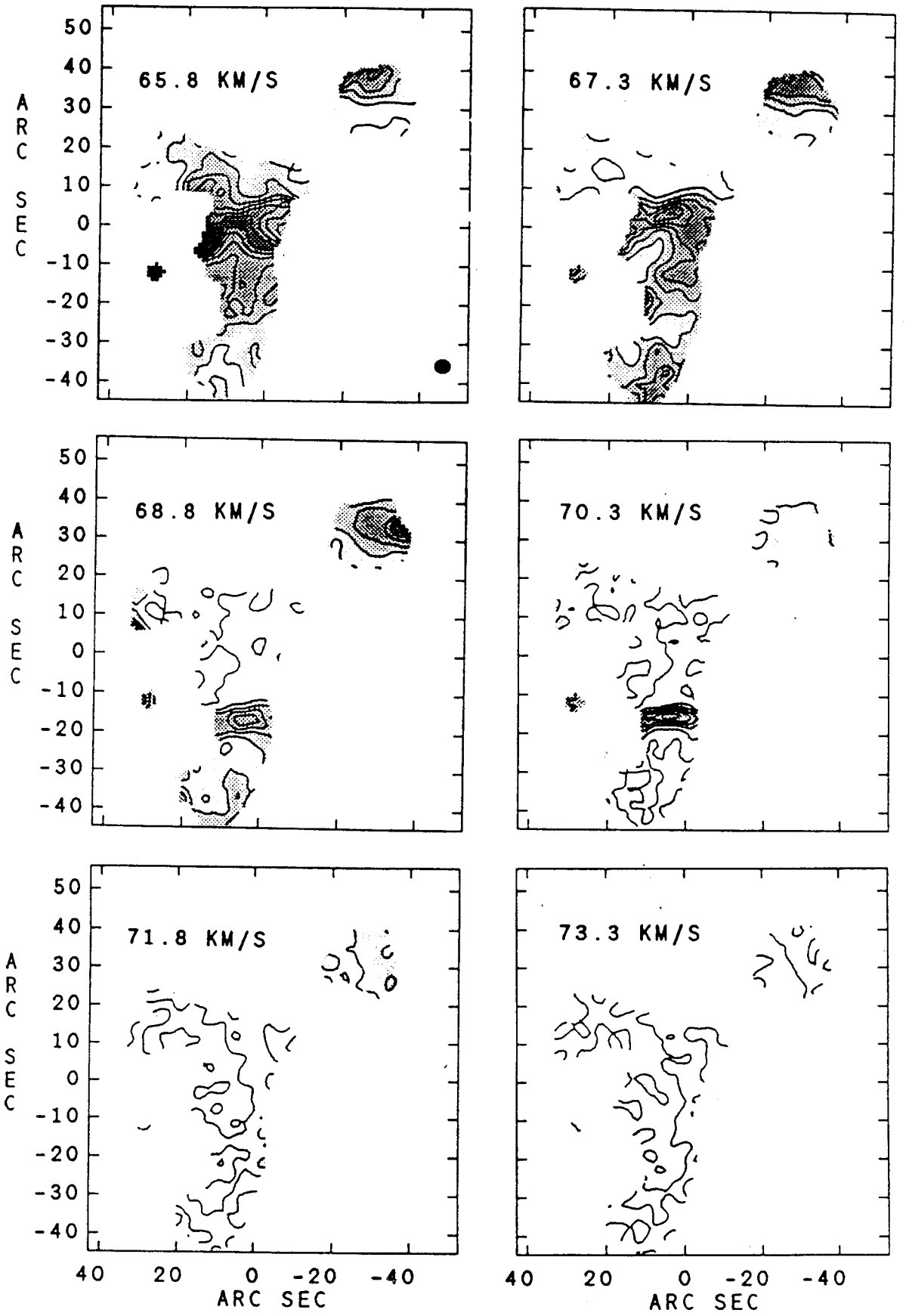
65.8 KM/S
67.3 KM/S
68.8 KM/S
70.3 KM/S
71.8 KM/S
73.3 KM/S
ARC SEC
50
40
30
20
10
0
-10
-20
-30
-40

Fig. 5b

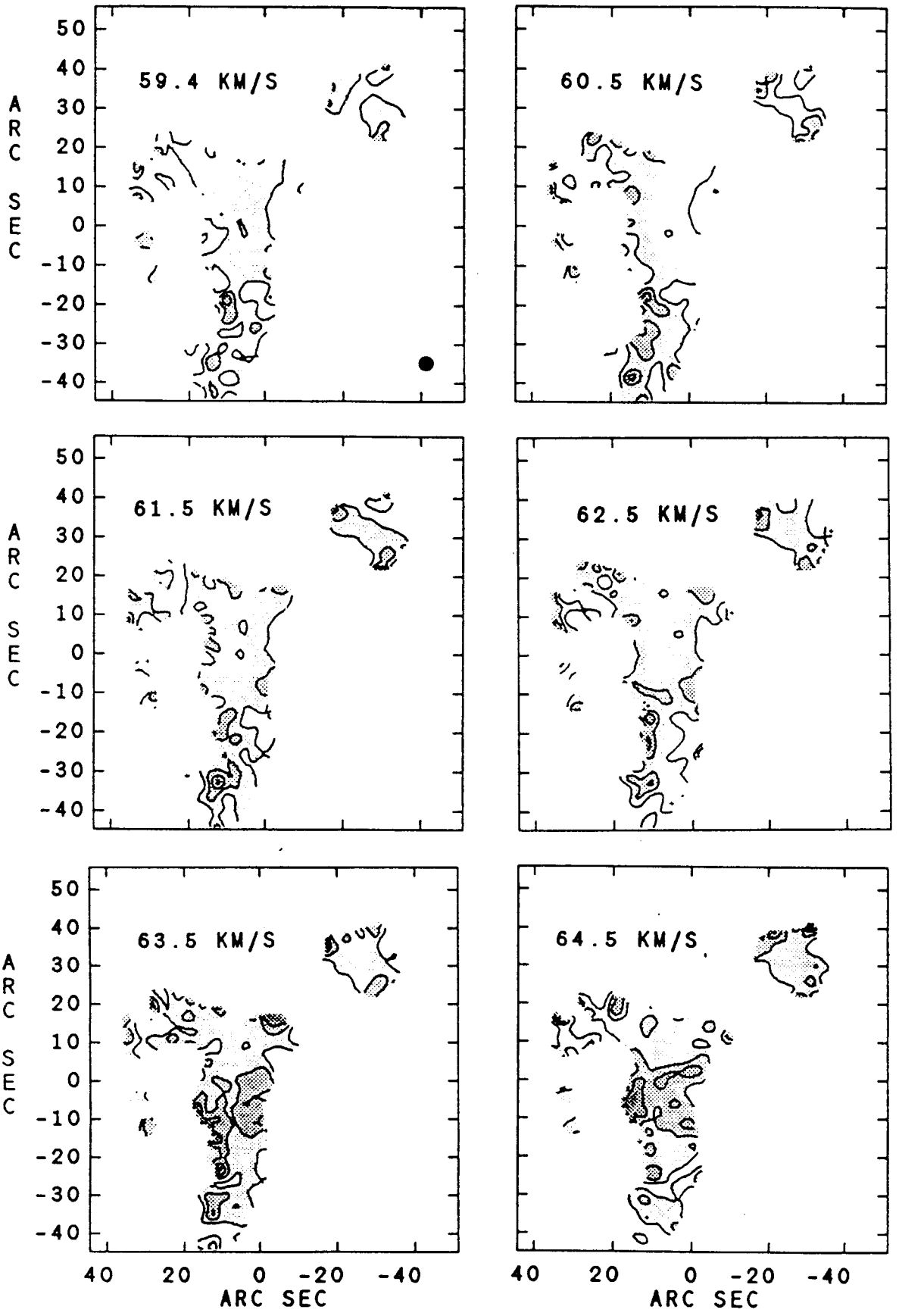
59.4 KM/S
60.5 KM/S
61.5 KM/S
62.5 KM/S
63.5 KM/S
64.5 KM/S
ARC SEC
50
40
30
20
10
0
-10
-20
-30
-40

Fig. 6a

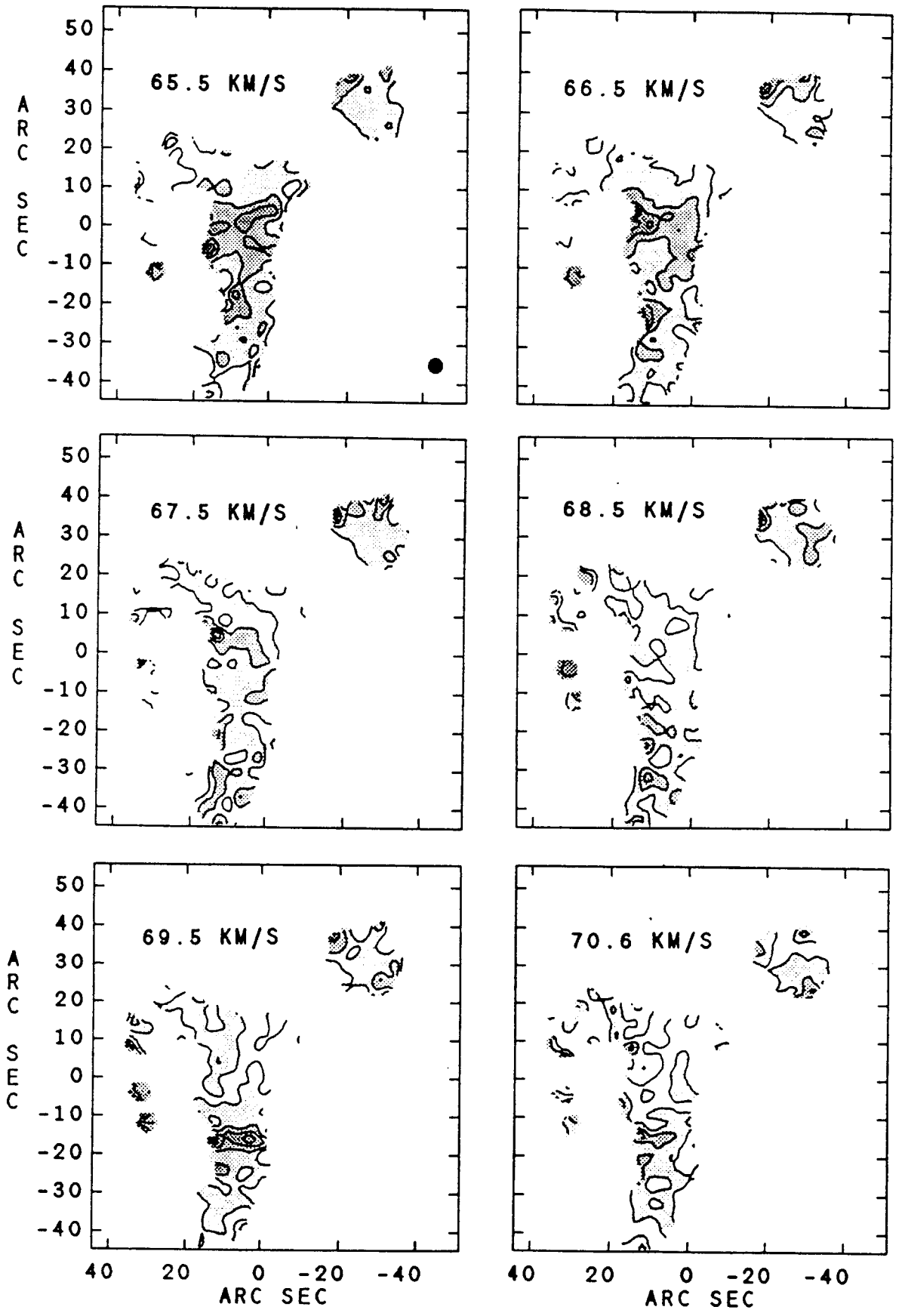
65.5 KM/S
66.5 KM/S
67.5 KM/S
68.5 KM/S
69.5 KM/S
70.6 KM/S
ARC SEC
50
40
30
20
10
0
-10
-20
-30
-40
40
20
0
-20
-40
ARC SEC

Fig. 6b

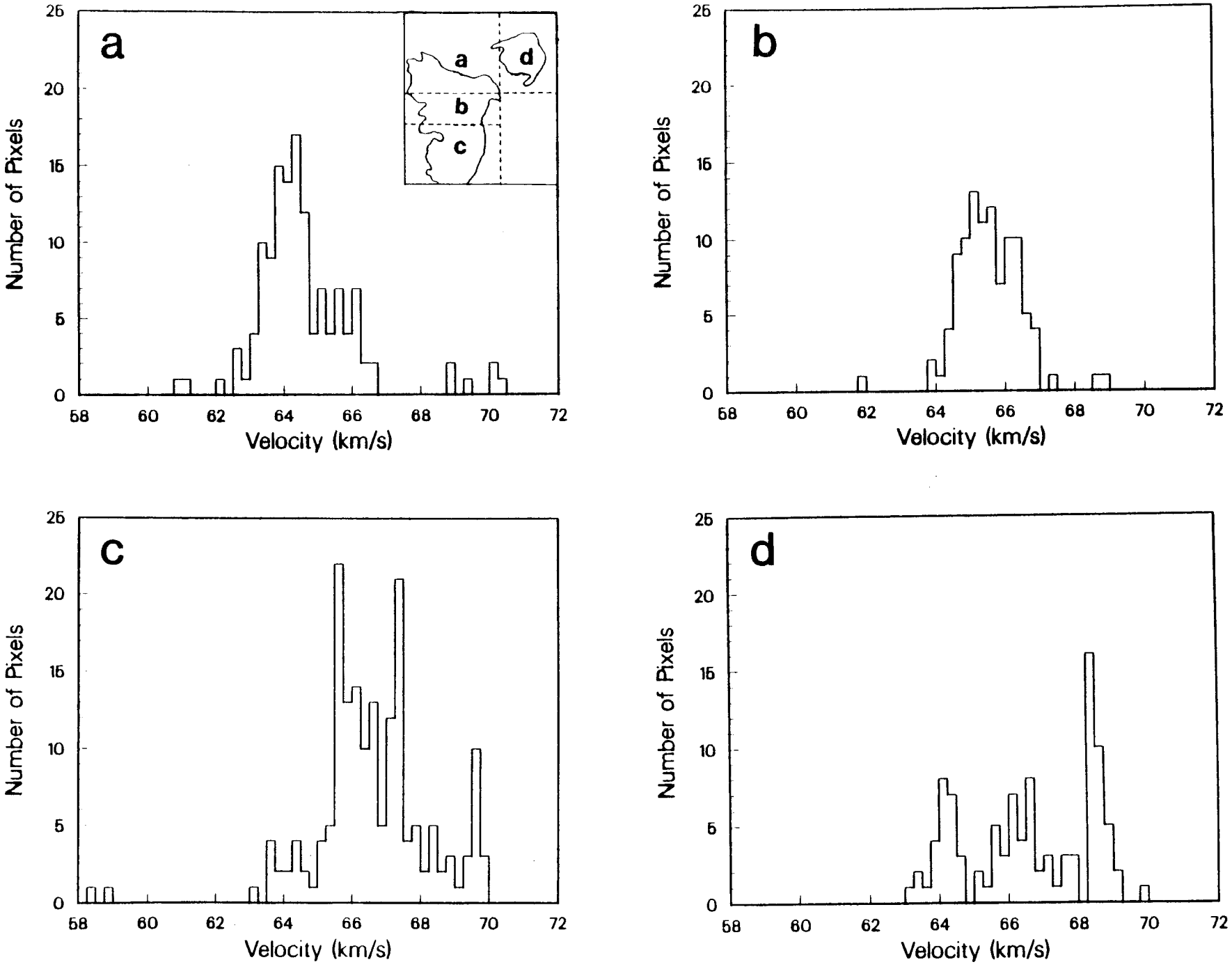
a
b
c
d
Number of Pixels
Velocity (km/s)
0
5
10
15
20
25
58
60
62
64
66
68
70
72

Fig. 7